Proceedings of CONF-CIAP 2026 Symposium: International Conference on Atomic Magnetometer and Applications
DOI: 10.54254/2753-8818/2026.HZ30831

Visual Detection of Water Salinity Based on the Transport of Intensity Equation

Chenzhong Luo

YK Pao School, Shanghai, China
s16108@ykpaoschool.cn

Abstract. Traditional salinity detection techniques, such as conductivity-based methods and optical refraction approaches, exhibits many limitations, including high equipment costs, the necessity for contact-based measurements, and poor environmental adaptability. This study proposes a novel non-interferometric optical measurement method based on the Transport-of-Intensity Equation (TIE) to solve these aforementioned issues. Theoretically, the phase shift of a light wave passing through a water medium is directly proportional with the refractive index, which can then be used to calculate the water salinity. Based on this principle, the study uses TIE to reconstruct a two-dimensional phase distribution from light intensity, from which the refractive index distribution are calculated, therefore determining salinity levels of the water body. In the experiments conducted, a combination of static and dynamic experiments was conducted to verify the feasibility of the proposed method, gaining valuable insights for its future practical application. The TIE-based technique introduced in this study presents several advantages over conventional techniques, such as non-contact operation, full-field rapid imaging, simple setup, and low cost—making it particularly suitable for the development of future water quality monitoring networks.

Keywords: Computational Imaging, Phase Imaging, the Transport-of-Intensity Equation

1. Introduction

In the modern world today, global water scarcity and pollution has already become a major environmental crisis. Annually, over 420 billion cubic meters of wastewater contaminates approximately 5.5 trillion cubic meters of freshwater, which exceeds 14% of the global total runoff. This immense scale makes water quality monitoring an urgent priority, with salinity, or the total dissolved salt concentration, being a key indicator influencing water quality. The detection of salinity is crucial for assessing ecological environments, agricultural production, drinking water safety, and industrial applications.

Salinity directly impacts aquatic survival; for instance, corals and fish are highly sensitive to salinity fluctuations, where deviations beyond tolerance can cause population decline or even ecosystem collapse [1]. In river deltas and coastal ecosystems like mangrove forests, salinity monitoring helps track seawater intrusion and wetland degradation. Furthermore, climate-induced sea-level rise increases freshwater salinization risks in coastal areas, making salinity detection vital for early-warning systems [2].

DOI: 10.54254/2753-8818/2026.HZ30831

In agriculture, irrigation with high-salinity water can cause soil salinization and reduce crop yields, particularly in arid regions [3]. For example, staple crops such as wheat and rice are quite sensitive to soil salt levels, which means long-term use of high-salinity irrigation water can reduce soil productivity by over 30% [4]. Therefore, salinity detection is essential for optimizing irrigation strategies and ensuring food security. In aquaculture, precise salinity management is critical as well, since species like shrimp and salmon have rigorous salinity requirements. Fluctuations in salinity can induce stress in cultured organisms, weaken immunity, and heighten disease risks [5].

Furthermore, elevated salinity in drinking water raises health risks including hypertension and cardiovascular diseases [6]. Industrially, wastewater discharge or seawater intrusion can elevate freshwater salinity, requiring monitoring to identify pollution sources and guide cleaning efforts [7]. High-salinity water also accelerates pipeline and boiler corrosion, increasing maintenance costs. Salinity data can further aid marine research; NASA's Aquarius mission analyzed ocean circulation and climate via global salinity monitoring [8].

Due to the importance of water salinity, to meet the demands for salinity measurement across various scenarios, the scientific and engineering communities have developed numerous mature monitoring solutions. These include refractometers, conductivity meters, and remote sensing technologies, which contributed to the formulation of scientific water resource management strategies and the achievement of sustainable development goals.

The evaporation method [9], while simple, is time-consuming and temperature-sensitive, limiting its use to mainly calibration. Refractometry measures salinity via refractive index variations and enables rapid detection in marine applications [10]. Conductivity methods measuring free electrons within the solution, reflecting the number of dissolved sodium ions and therefore reflecting the water salinity. The conductometer used in this method offers fast response and operational ease, making it one of the most widely used apparatus [9]. Remote sensing supports large-scale salinity monitoring, with an example being NASA's Aquarius mission, which utilizes microwave radiometers to gain valuable data on ocean salinity [10]. However, these conventional methods face limitations such as electrode contamination, maintenance costs, or contact requirements, while remote sensing face problems in restricted spatial resolution in near-ground applications. Furthermore, most methods provide only one-dimensional data, as 2D techniques remain complex and costly, limiting their usage.

In recent years, with advancements in optical technology, label-free, non-contact, and high-resolution two-dimensional imaging methods have gained attention. One example is Digital Holographic Microscopy (DHM) [11]. This method splits a light beam into two: one illuminates the object to record its information, while the other serves as a reference beam. The interference pattern formed by the superposition of these two beams is captured by a digital sensor, and the resulting fringe information contains details about the object, enabling the reconstruction of its phase information [12,13]. By computationally reconstructing phase images, local variations in the refractive index of the water can be obtained. Since salinity directly affects the refractive index, phase information can indirectly facilitate two-dimensional imaging of salinity distribution.

However, DHM has notable limitations. First, the system demands high stability in the optical path and is highly susceptible to environmental vibrations or temperature, mainly due to its reliance on precise interference patterns. Even minor fluctuations can damage observation quality significantly. Second, achieving high-quality holographic images typically requires complex system configurations, including high-precision lasers, interferometric optical paths, and stable reference arms. Furthermore, for transparent samples or liquids with low phase contrast, DHM reconstructions

DOI: 10.54254/2753-8818/2026.HZ30831

may suffer from strong background interference and fringe artifacts, affecting quantitative accuracy [14-16].

To address these limitations, this study proposes a non-contact, cost-effective environmentally robust, and two-dimensional salinity detection method using the Transport of Intensity Equation (TIE) [17]. In this method, we used one or a few images' intensity variation to reconstruct the phase distribution through TIE. After the phase information of the sample is obtained, we can derive the refractive index distribution of the water body, which allows for measurement of local salinity levels.

Moreover, it does not require expensive instruments—only a few lenses and an industrial camera are needed to determine water salinity.

This technology is not limited to salinity detection. As it does not rely on staining or contact probes, it is also applicable to various other soluble pollutants. Its potential for use in complex aquatic environments is substantial, offering broad prospects for the future of water quality detection.

2. Theoretical basis

2.1. Angular spectrum propagation

The propagation of light waves in free space can be analyzed using the angular spectrum method. The central idea of this approach is to decompose the initial light field into plane waves traveling in different directions (referred to as angular spectrum components), study the changes these plane waves undergo during propagation, and finally recombine them to synthesize the propagated light field. This process involves Fourier transforms, the Helmholtz equation, and the propagation characteristics of plane waves.

Consider a monochromatic plane wave propagating along the wave vector $\vec{k}$, where $|\vec{k}| = 2\pi/\lambda$, with directional cosines $(\alpha,\ \beta,\ \gamma)$. Denoting the light field distribution at the plane $z = 0$ as $U(x,\ y,\ z)$, then, the complex representation of this plane wave would be [18] :

$$P(x,\ y,\ z;t) = e^{j\left(\vec{k}\bullet\vec{r}-2\pi vt\right)} = e^{j\vec{k}\bullet\vec{r}} \tag{1}$$

In which, $\vec{r} = x\hat{x} + y\hat{y} + z\hat{z}$ is the positional vector (the $\hat{}$ sign showing it's a unit vector), while $\vec{k} = \frac{2\pi}{\lambda}\left(\alpha\hat{x} + \beta\hat{y} + \gamma\hat{z}\right)$, where we can disregard it's time-dependent nature. Henceforth, we can write the direction cosine of its propagation as $\alpha = \lambda f_X$, $\beta = \lambda f_Y$,and $\gamma = \sqrt{1 - (\lambda f_X)^2 - (\lambda f_Y)^2}$.

Thus, the following equation can be yielded:

$$S\left(\frac{\alpha}{\lambda},\ \frac{\beta}{\lambda};\ 0\right) = \iint_{-\infty}^{\infty} U(x,\ y,\ 0)e^{-j2\pi\left(\frac{\alpha}{\lambda}x+\frac{\beta}{\lambda}y\right)}dxdy \tag{2}$$

This is called the angular spectrum disturbing $U(x,\ y,\ 0)$ .Similarly, we can transform this function on the z-plane to

DOI: 10.54254/2753-8818/2026.HZ30831

$$S\left(\frac{\alpha}{\lambda},\ \frac{\beta}{\lambda};\ z\right)=\iint_{-\infty}^{\infty}U\left(x,\ y,\ z\right)e^{-j2\pi\left(\frac{\alpha}{\lambda}x+\frac{\beta}{\lambda}y\right)}dxdy \tag{3}$$

By substituting the Helmholtz equation into the angular spectrum representation, we obtain:

$$\frac{d^2}{dz^2}S\left(\frac{\alpha}{\lambda},\ \frac{\beta}{\lambda};\ z\right)+\left(\frac{2\pi}{\lambda}\right)^2\left[1-\alpha^2-\beta^2\right]S\left(\frac{\alpha}{\lambda},\ \frac{\beta}{\lambda};\ z\right)=0 \tag{4}$$

A fundamental solution of the above equation can be represented as below. This solution also gives the evolution pattern of angular spectrums with respect to its propagation distance:

$$S\left(\frac{\alpha}{\lambda},\ \frac{\beta}{\lambda};\ z\right)=S\left(\frac{\alpha}{\lambda},\ \frac{\beta}{\lambda};\ 0\right)e^{j\frac{2\pi}{\lambda}z\sqrt{1-\alpha^2-\beta^2}} \tag{5}$$

Henceforth, we define the angular spectrum transfer function (ASTF) as:

$$H\left(f_X,\ f_Y;\ z\right)=e^{j\frac{2\pi}{\lambda}z\sqrt{1-\left(\lambda f_X\right)^2-\left(\lambda f_Y\right)^2}} \tag{6}$$

Equation (10) fully describes the modulation effect of propagation in free space on each angular spectrum components. Thus:

$$U\left(x,\ y,z\right)=\iint_{-\infty}^{\infty}H\left(f_X,\ f_Y;\ z\right)S\left(f_X,\ \ f_Y;0\right)e^{j2\pi\left(f_Xx+f_Yy\right)}df_Xdf_Y \tag{7}$$

Here, certain physical phenomena require clarification. For propagating waves, when $f_X^2+f_Y^2<1/\lambda^2$, ASTF will cause phase modulation. However, when $f_X^2+f_Y^2>1/\lambda^2$, $H\left(f_X,f_Y;z\right)=e^{-\frac{2\pi}{\lambda}z\sqrt{\left(\lambda f_X\right)^2+\left(\lambda f_Y\right)^2-1}}$, which is a positive real number. This causes the wave components to decay rapidly during propagation, which led to those components being referred to as evanescent waves. The transfer function exhibits an abrupt change at the spatial frequency $f_X^2+f_Y^2=1/\lambda^2$, corresponding to the propagation cutoff frequency.

2.2. Transport of intensity equation

Consider a monochromatic optical wave field $U\left(x,y,z\right)=E\left(x,y,z\right)=A\left(x,y,z\right)e^{j\phi\left(x,y,z\right)}$, where A represents the amplitude, and ϕ represents the phase. Assume the optical field mainly propagates along the z-axis, under paraxial approximation (small-angle propagation), the field satisfies the Helmholtz equation, where the term $\frac{\partial^2E}{\partial z^2}$ is small enough to neglect. For a plane wave propagating in the positive z-direction (i.e., $f_X=f_Y=0$), the transfer function simplifies to $H\left(0,0;z\right)=e^{j\frac{2\pi}{\lambda}z}=e^{jkz}$. Therefore, during propagation along the z-axis, the phase change is mainly affected by e^{jkz} . Expanding the Laplace operator ∇^2 in the Helmholtz equation will yield:

$$2ik\frac{\partial E}{\partial z}=-\nabla_\perp^2E \tag{8}$$

Where, $\nabla_\perp^2$ denotes the transverse Laplacian operator, and $k=\frac{2\pi}{\lambda}$ is the wave number. At this point, the amplitude can be expressed as $I=E\left(x,\ y,\ z\right)E^*\left(x,y,z\right)$, where * represents the

DOI: 10.54254/2753-8818/2026.HZ30831

complex conjugate. Substituting it into the above equation yields [17]:

$$\frac{\partial I}{\partial z} = -\frac{\lambda}{2\pi}\nabla \bullet \left(I\nabla\phi\right) \tag{9}$$

Which is the final form of the Transport of Intensity Equation.

2.3. Solving the Transport of Intensity Equation

Since the proposal of the Transport of Intensity Equation (TIE), its solution has consistently posed a significant challenge. One common approach for solving it is the Fourier transform method, which is also the solution method adopted in this study. First, a Fourier transform is applied to both sides of the equation, yielding:

$$\frac{\partial \mathcal{F}\{I(x,\,y,\,z)\}}{\partial z} = -\frac{\lambda}{2\pi}\mathcal{F}\left\{\nabla \bullet \left(I\left(x,\,y,\,z\right)\nabla\phi\left(x,\,y,\,z\right)\right)\right\} \tag{10}$$

Utilizing the properties of Fourier transformations, we can get

$$\mathcal{F}\left\{\nabla \bullet \left(I\nabla\phi\right)\right\} = j\left\{u\mathcal{F}\left\{I\frac{\partial\phi}{\partial x}\right\} + v\mathcal{F}\left\{I\frac{\partial\phi}{\partial y}\right\}\right\} \tag{11}$$

Substituting $\hat{I}\left(u,\,v\right) = \mathcal{F}\{I\left(x,\,y,\,z_0\right)\}$, $\mathcal{F}\left\{\frac{\partial\phi}{\partial x}\right\} = ju\mathcal{F}\left\{\phi\right\}$, and $\mathcal{F}\left\{\frac{\partial\phi}{\partial y}\right\} = jv\mathcal{F}\left\{\phi\right\}$ into equation (11) and rearrange it, we can yield a Fourier distribution of the phase $\widehat{\phi}\left(u,\,v\right)$:

$$\widehat{\phi}\left(u,\,v\right) = \frac{-2\pi}{\lambda(u^2+v^2)}\frac{\partial\hat{I}(u,\,v)}{\partial z}\frac{1}{\hat{I}(u,\,v)} \tag{12}$$

After a reverse Fourier transformation, we would get the equation

$$\phi\left(x,\,y\right) = \mathcal{F}^{-1}\left(\widehat{\phi}\left(u,\,v\right)\right) = \mathcal{F}^{-1}\left(\frac{-2\pi}{\lambda(u^2+v^2)}\frac{\partial\hat{I}(u,\,v)}{\partial z}\frac{1}{\hat{I}(u,\,v)}\right) \tag{13}$$

Which we can utilize the Fast Fourier Transformation (FFT) in MATLAB to solve.

3. Principle-based simulation

3.1. Basic optical path design

Since this experiment requires the reconstruction of the object's phase information and involves camera translation for image acquisition, a 4f optical system is employed to ensure consistent image dimensions across multiple captures. The LED laser source is turned into a parallel beam using convex lens 1, which illuminates the specimen to encode optical information. To capture the full profile of the water sample, the system is configured as a demagnification system, making the object seem smaller through the camera than its actual size. By introducing minor axial displacement of the camera, intensity distributions at two distinct planes are recorded, enabling the derivation of the axial intensity derivative through numerical differentiation in post-processing.

DOI: 10.54254/2753-8818/2026.HZ30831

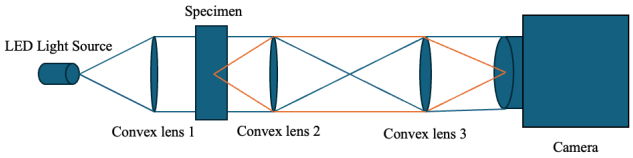

Figure 1. Simple structure of the optical path used in the experiment

3.2. Simulations and analysis

Before conducting real-life experiments, we first need to test the feasibility of the MATLAB code, which is achieved through simulation experiments. We simulate a phase object by assuming an ideal phase object whose phase distribution is shown in Fig. 2(b), and its intensity distribution is illustrated in Fig. 2(a). In the simulation, we used a pixel size of 2μm, a wavelength of 633 nm, and a defocus distance of 10μm. The intensity distribution captured at the defocus position is displayed in Fig. 2(c), while Fig. 2(d) presents the distribution of the axial intensity derivative.

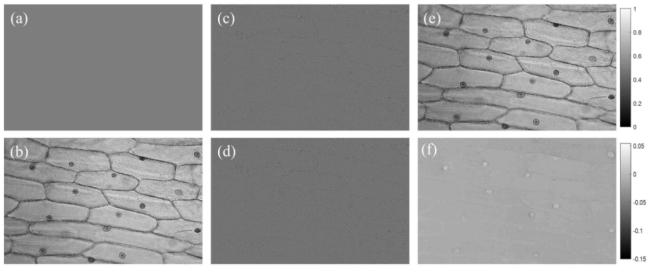

Figure 2. Simulation results under Gaussian intensity distribution (when there is a high light source coverage). (a) In-focus image, (b) Phase distribution of the simulated phase object, (c) Intensity distribution of the object at the defocused plane, (d) Axial intensity derivative, (e) Reconstructed phase distribution of the object, (f) The difference between the reconstructed phase distribution and the standard value

By applying the fast Fourier transform method described in Section 2.3, the phase distribution can be efficiently solved, with the result shown in Fig. 2(e). It can be observed that the phase information obtained in Fig. 2(e) closely matches the true phase information in Fig. 2(b), exhibiting identical features. To quantitatively evaluate the reconstruction performance, a comparison was made with the theoretical values from Fig. 2(b), yielding the error distribution depicted in Fig. 2(f). The results indicate that the errors are minimal, with the minor inaccuracies primarily concentrated at the edges and nuclei of the cells.

However, when a illumination source which has a non-uniform and localized intensity is shone on the subjects, the simulation results are shown in Fig. 4. It can be observed that the reconstructed result in Fig. 4(e) shows quite a large difference from the theoretical values in Fig. 4(b). This is primarily because of the presence of numerous near-zero intensity values in the captured intensity distribution at the focal plane, which causes significant computational errors during the reconstruction process.

DOI: 10.54254/2753-8818/2026.HZ30831

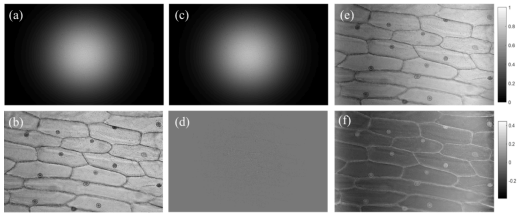

Figure 3. Simulation results under Gaussian intensity distribution (when there is a high light source coverage). (a) In-focus image, (b) Phase distribution of the simulated phase object, (c) Intensity distribution of the object at the defocused plane, (d) Axial intensity derivative, (e) Reconstructed phase distribution of the object, (f) The difference between the reconstructed phase distribution and the standard value

Therefore, the results of the simulation experiments indicate that in the final experimental setup, the illumination should uniformly cover the entire field as much as possible to minimize the disturbance of near-zero intensity values on the calculations, which may compromise the results.

4. Experiments and analysis

4.1. Experimental optical path

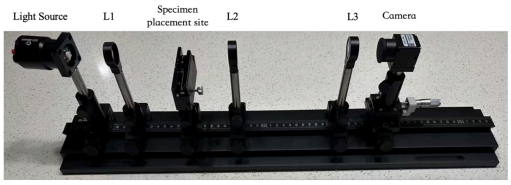

Figure 4. Experimental optical path diagram

For the sake of clarity, the focal lengths of the lenses in the optical path are denoted as follows: lens L1 as F1, lens L2 as F2, and lens L3 as F3. Since the Fourier plane needs to be reconstructed between lenses L1 and L2, it is essential to ensure F1 = F2 in this experiment. The distance between the light source and lens L1 should be exactly F1. Correspondingly, the distance between lens L1 and the sample placement position should also be F1. The distance between lens L2 and the sample placement position should be F2, while lens L3 should be positioned at a distance of F3 + F2 from lens L2. Furthermore, the distance between lens L3 and the camera should be F2. As the optical path in this experiment is configured as a demagnification system, F3 must be greater than F1 and F2. Therefore, lenses L1 and L2 with a focal length of 50.8 mm and lens L3 with a focal length of 100 mm were used in this experiment. Also, a green laser with a wavelength of 528 ± 10 nm served as the light source, and a camera with a resolution of 3072 × 2048 pixels and a maximum frame rate of 70 fps was used.

4.2. Experiment operation procedure for static/dynamic specimens

1. Power up the laser with a power supply, connect the camera to the computer, and enable auto-exposure in the camera driver software.

2. Adjust the optical path, turn on the camera, and fine-tune the light source intensity based on real-time image feedback from the camera.

DOI: 10.54254/2753-8818/2026.HZ30831

3. Static Specimens: Place a static specimen at the designated sample position in the optical path. Due to the demagnifying nature of the setup, it is recommended to use specimens with clearly visible features. In this experiment, pine stem sections and bee wings were used as specimens.

Dynamic Specimens: Replace the sample in the optical path with two optical cells filled with identical water samples (in this experiment, tap water was directly used). Capture an image at this point to serve as the in-focus reference image.

4. Adjust the translation stage beneath the camera until the specimen's image appears sharpest in the driver software, then capture an image in BMP format.

5. Increase the reading of the translation stage by 15 (equivalent to 15 μm) and capture another BMP-format image.

6. Static Specimens: Rename the two images, input them into the MATLAB code, and execute the code. A clear representation of the three-dimensional morphological features of the specimen in the phase map indicates a correctly configured optical path.

Dynamic Specimens: Add salt to the right-side optical cell. Continue recording until the salt has fully diffused and dissolved before stopping the video.

7. Dynamic Specimens: Input the captured reference image and the recorded video into the MATLAB code, and execute the code. During computation, the initial image serves as the in-focus reference, while each frame of the video functions as a defocused image. Consequently, each frame can be processed to generate a corresponding phase map. Collectively, these phase maps form a time-lapse sequence of phase changes, effectively representing the dynamic salinity distribution over time.

4.3. Static solid sample experiment

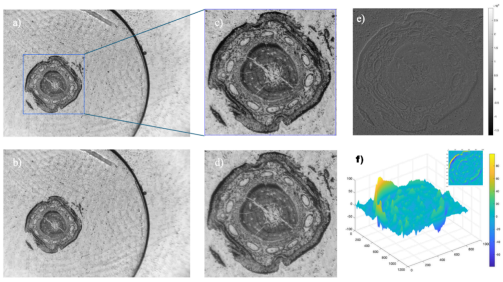

Figure 5. Phase reconstruction of a pine stem slice. (a) Original focused image, (b) Original defocused image, (c) Selected region from the in-focus image used for computation, (d) Selected region from the defocused image used for computation, (e) Axial intensity derivative of the object, (f) Reconstructed 3D phase distribution of the object with its planar view shown in the upper-right corner

Before conducting dynamic experiments on water, imaging of static samples was first performed. Since the entire imaging system is a demagnifying setup, relatively large samples—namely, a pine stem slice and a bee wing specimen—were used for testing. Under focused conditions, the distribution of the entire pine stem slice can be observed, as shown in Fig. 5(a). To reduce computational costs, only the region of interest was selected for reconstruction. For this sample, the central area containing substantive structures was chosen, as indicated by the blue box in Fig. 5(a), with the corresponding magnified view displayed in Fig. 5(c). Due to the characteristics of the Transport of Intensity Equation (TIE), at least two images of the object at different focal planes are required. Therefore, an image of the object distribution on a defocused plane was also captured, as

DOI: 10.54254/2753-8818/2026.HZ30831

shown in Fig. 5(b). Similarly, the central region was selected for reconstruction, as shown in Fig. 5(d). Fig. 5(e) presents the axial intensity derivative of the object through a greyscale quantification, where darker areas represents a lower axial intensity derivative and vice versa. This reflects the rate of intensity variation along the propagation direction, serving as the core basis for phase retrieval through TIE. Finally, Fig. 5(f) displays the reconstructed phase distribution, quantified along the z-axis, or the height, in the 3D plot, validating the effectiveness of TIE in phase imaging of biological tissues (pine stem slice). It can be observed that the phase map of the selected region retains most of the features of the original object. However, the transparent regions of the original object presents significantly lower phase values than the non-transparent areas. Since the phase value maintains a quantitative proportional relationship with the physical height of the object (assuming a nearly uniform refractive index for the same sample), it can be inferred that the actual height of the transparent regions is substantially lower than that of the non-transparent regions. This is information that conventional imaging methods, such as that in Fig. 5(a), cannot provide.

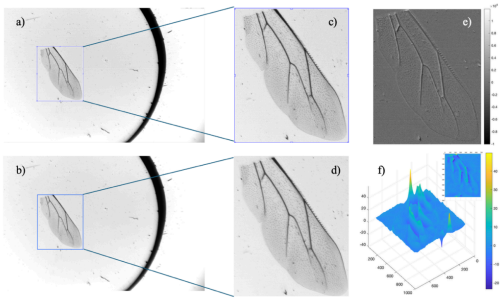

Figure 6. Phase reconstruction of a bee wing specimen. (a) Original focused image, (b) Original defocused image, (c) Selected region from the in-focus image used for computation, (d) Selected region from the defocused image used for computation, (e) Axial intensity derivative of the object, (f) Reconstructed 3D phase distribution of the object with its planar view shown in the upper-right corner

Similarly, in the bee wing experiment, one in-focus image and one defocused image were captured to compute the phase distribution, as shown in Figs. 6(a) and 6(b), respectively. Only the region containing the specimen was selected for phase reconstruction, corresponding to the areas marked by blue boxes in Figs. 6(a) and 6(b). Magnified views of the selected regions are presented in Figs. 6(c) and 6(d). To derive the phase of the specimen, the axial intensity derivative was first calculated, as illustrated in Fig. 6(e). The final reconstructed phase distribution is quantified by the z-axis values in the 3D plot, as shown in Fig. 6(f). From the phase map, we can see the phase values in the transparent regions of the specimen are significantly lower than those in the non-transparent regions. Thus, it can be inferred that the physical height of the transparent regions is substantially lower than that of the non-transparent regions. This further demonstrates that phase reconstruction via TIE can reveal information inaccessible to conventional imaging methods such as that in Fig. 6(a).

DOI: 10.54254/2753-8818/2026.HZ30831

4.4. Static liquid sample experiment

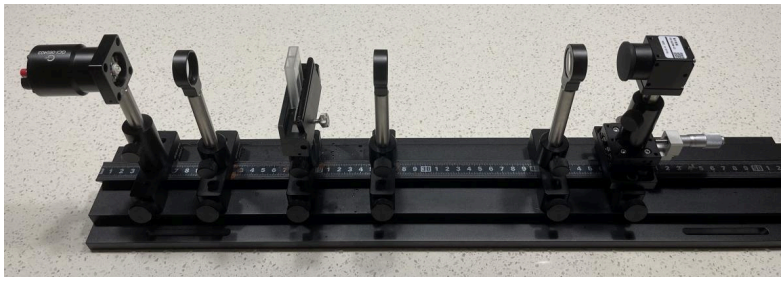

Figure 7. Experimental setup with optical cell

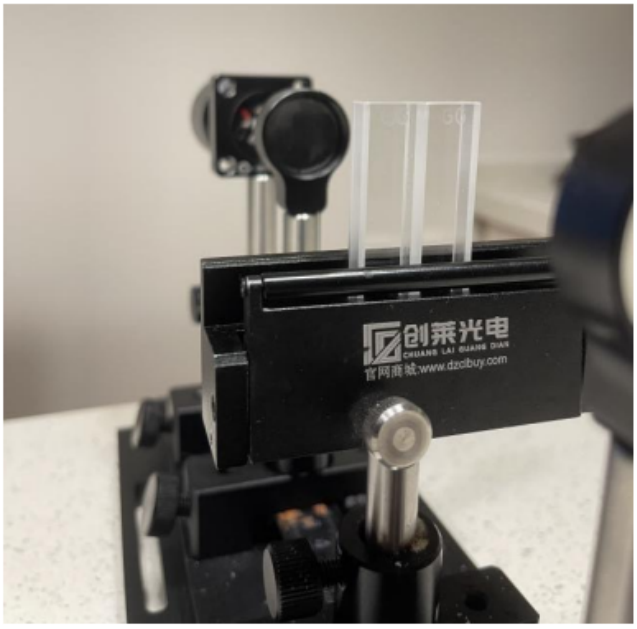

Figure 8. Optical cell used in experiment

Before conducting dynamic experiments on water samples, static two-dimensional imaging of water samples was performed. Figure 7 illustrates the optical setup, which is identical to the setup in Figure 4, except it incorporates an optical cell instead of specimen samples. Among the four vertical surfaces of the optical cell, two opposing surfaces are transparent, while the other pair of opposing surfaces uses frosted glass, as detailed in Figure 8. Since the optical cell is colorless and transparent along the axial direction of the light path, and water is also a colorless transparent liquid, capturing a well-focused image is particularly challenging due to the considerable thickness of the optical cell (5 mm in this experiment, which remains unchanged when filled with water). To address this, the experiment was designed using a comparative approach: two optical cells were employed, with the left cell filled with tap water and the right cell filled with salt solution. The captured images are shown in Figures 9(a) and 9(b).

DOI: 10.54254/2753-8818/2026.HZ30831

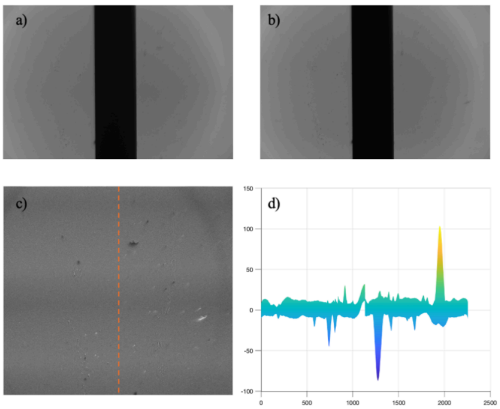

Figure 9. Phase reconstruction of low salinity water (left: tap water, right: salt solution). (a) Selected in-focus image, (b) Corresponding defocused image, (c) Axial intensity derivative of the object (the left of the dashed line represents tap water, while the right represents salt solution; the black areas corresponding to the optical cell walls have been removed for clearer visualization), (d) Reconstructed phase distribution of the object (shown from one perspective of the 3D representation)

Figures 9(a) and 9(b) present the captured in-focus and defocused images of the optical cell, respectively. The axial intensity derivative of the optical cell, shown in Figure 9(c), was then used to calculate the phase distribution depicted in Figure 9(d). To better visualize the results, the central regions corresponding to the optical cell walls are omitted in Figures 9(c) and (d). Here, we can observe that the phase values in the right region are higher than those in the left region. In figure 9(d), we can observe two large spikes on the phase distribution graph, which may be attributed to larger contaminants introduced by the household experimental environment. Notably, a prominent negative-phase spike appears in the right region of the phase map. This anomaly arises because the corresponding impurity is absent in the in-focus image (Figure 9(a)) but becomes noticeable in the defocused image (Figure 9(b)), leading to computational misinterpretation as an anomalous negative phase. One probable cause is the time interval between capturing Figures 9(a) and 9(b), during which new impurities may have entered the imaging area due to the non-sterile experimental conditions.

The specific relationship between the reconstructed phase ϕ and the salinity of the solution will be analyzed and discussed in greater detail below.

The reconstructed phase ϕ is linearly related to the refractive index of the liquid through the following formula:

$$\phi = \frac{2\pi L}{\lambda} N \tag{14}$$

Where L is the thickness of the optical cuvette, λ is the wavelength of the light source, and N is the refractive index of the solution. The refractive index can be determined:

$$N = N_0 + kC \tag{15}$$

In Equation (15), N represents the refractive index of the solution, N_0 denotes the refractive index of the solvent, C is the solute concentration in percentage, and k is the specific refractive index increment dependent on the solute-solvent pair. For saline solutions in water, the k value

DOI: 10.54254/2753-8818/2026.HZ30831

typically ranges between 0.0018 and 0.002. With the refractive index of pure water N_0 being approximately 1.333 and the solute concentration of the saturated saline solution used in this study (Fig. 9) being about 26%, the refractive index of the saturated saline solution can be calculated as $1.333 + 0.0019 \times 26 = 1.3798$, differing from that of pure water by only 0.0498. Additionally, as the experiment was conducted in summer, elevated temperatures may reduce the density of the saline solution, leading to a slight decrease in its refractive index. In summary, while the phase difference between the saline solution and tap water is expected to be small, the corresponding refractive index distribution can still be quantitatively derived from the phase distribution. This enables the determination of the two-dimensional salinity distribution based on reference data, with the spatial variation trend of salinity aligning directly with that of the phase distribution.

4.5. Dynamic water experiment

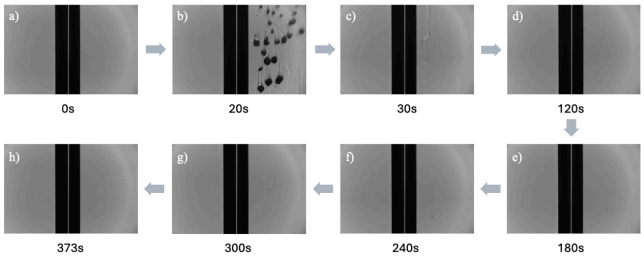

Figure 10. Recording the formation process of saline solution after adding salt to the right side using traditional optical methods. (a) State before adding salt to the right side, (b-c) Process of adding salt to the right water body, (d-h) Gradual formation of saline solution on the right side

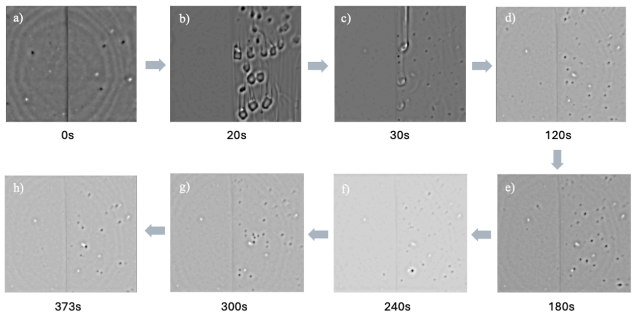

Figure 11. Dynamic phase reconstruction of the water body based on Figure 10. (a) Phase map before adding salt to the right side, (b-c) Phase maps during the salt addition process, (d-h) Phase maps during the formation of the saline solution on the right side

After multiple verifications of the feasibility of this experiment, we conducted dynamic experiments on water samples at last. In the experiment, the left water body served as the control group, which consistently maintained as tap water. The right water body, initially tap water, transitioned into a saline solution through the addition of salt, with its phase changes recorded by video at a frame rate of 10 frames per second. It should be noted that the video frame rate is constrained by the camera's acquisition speed, directly affecting the final frame rate of the phase video, independent of the reconstruction processing speed. Figure 11 presents the frame-by-frame phase reconstruction from the dynamic experiment.

DOI: 10.54254/2753-8818/2026.HZ30831

Due to space limitations, only key frames are selected here to illustrate the results of the dynamic experiment. This experiment also used grayscale quantification, where brighter areas correspond to lower phase values and vice versa. The varying brightness in the images arises because, during the process of saving the phase data as a video, phase values were linearly mapped to the 0–255 range: the minimum value was mapped to 0, the maximum value to 255, and intermediate values were proportionally scaled within this interval. When objects with extremely high phase values were introduced, the maximum value increased sharply, causing areas that were previously not minimal to appear relatively darker and thus making the overall image brighter. Figure 11(a) shows the first frame of the video, displaying the phase map before salt was added to the right water body, where little difference in phase is observed between the two sides. Figures 11(b–c) depict the scenario during salt addition, where water surrounding the salt grains exhibits significantly higher phase values due to rapid surface dissolution. Additionally, it is noted in Figures 11(d–h) that after the salt grains are added, the right water body contains numerous points with extremely high phase values, markedly more than the left side. This occurs because bubbles trapped within the salt grains are released into the water during dissolution, and light passing through these bubbles travels a longer optical path, resulting in these phase spikes. In subsequent frames, as the salt further dissolves, the phase of the right water body gradually becomes higher than that of the left. Furthermore, the highly visible bubbles in Figure 11 are almost imperceptible in Figure 10, further demonstrating that phase reconstruction can capture details that are challenging to detect with conventional optical methods.

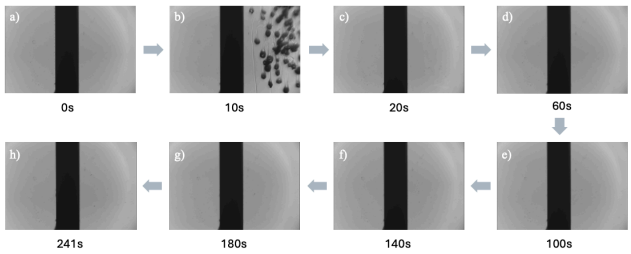

Figure 12. Recording the formation process of saline solution after adding salt to the right side using traditional optical methods for a second time. (a) State before adding salt to the right side, (b-c) Process of adding salt to the right water body, (d-h) Gradual formation of saline solution on the right side.

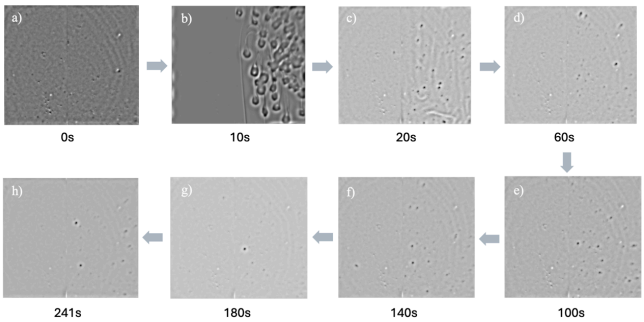

Figure 13. Figure 11 Dynamic phase reconstruction of the water body based on Figure 10. (a) Phase map before adding salt to the right side, (b-c) Phase maps during the salt addition process, (d-h) Phase maps during the formation of the saline solution on the right side

To ensure the stability of this method, we conducted multiple trials of the dynamic experiment. The phase results from another set of dynamic experiments are shown in Figure 11. Similarly, due to

DOI: 10.54254/2753-8818/2026.HZ30831

space constraints, only key frames are selected for presentation. Figure 11(a) shows the first frame of the video, depicting the phase when both sides contain tap water. Consistent with Figure 11(a), no significant phase difference is observed between the two sides. Figures 11(b–c) display the phase during salt addition, while Figures 11(d–h) illustrate the phase as the right side gradually transforms into a saline solution. Notably, several lines with elevated phase values appear in Figure 11(c), which are absent in Figure 11(c). These lines correspond to the lingering high-concentration saline trails left by the settling salt grains before diffusion. The high refractive index of these concentrated saline regions results in locally elevated phase values. Since conventional optical methods cannot capture refractive index information, the absence of these lines in Figure 11(c) is expected. This provides strong evidence for the feasibility of the method explored in this study.

5. Conclusion

This study mainly explored a method for measuring water salinity through phase reconstruction using the Transport of Intensity Equation (TIE). Compared to traditional methods, it offers advantages such as lower cost, non-contact operation, and relatively lenient environmental requirements. In the static sample experiments described in Section 4.3, the phase reconstruction method based on TIE successfully captured information difficult to obtain with conventional techniques—specifically, the height profile of the samples. In the static and dynamic water experiments detailed in Sections 4.4 and 4.5, TIE was further employed to successfully reconstruct the phase of water bodies, demonstrating that the phase of saline water is slightly higher than that of tap water. These results preliminarily validate the feasibility of the proposed method.

However, as the experiments were conducted in a non-laboratory setting without pre-treatment of water samples (e.g., filtration or degassing), impurities such as suspended particles or bubbles may have interfered with the measurements, as noted in Sections 4.4 and 4.5. Given the diverse composition of impurities in natural water bodies (e.g., algae in coastal areas or colloidal particles in rivers), future experiments will incorporate standardized pre-treatment procedures (such as filtration through 0.45μm membranes and ultrasonic degassing) to systematically evaluate the impact of different pre-treatment methods on salinity measurements in natural water. The results will also guide further refinement of the pre-treatment workflow. Such improvements are particularly relevant for long-term environmental monitoring, significantly enhancing data reliability. Additionally, the high ambient temperature during the experiments resulted in a relatively small phase difference between saline and tap water. Future work may adopt temperature compensation techniques to amplify phase contrast and improve data comparability.

Furthermore, since this method relies solely on light propagation to determine water salinity, it can be extended to detect other soluble pollutants, such as oils and esters. In summary, the TIE-based approach to water salinity measurement, with its numerous advantages and potential for broader application, holds promising prospects for future development and practical implementation.

References

[1] Hoegh-Guldberg O, Mumby P J, Hooten A J, et al. Coral reefs under rapid climate change and ocean acidification [J]. science, 2007, 318(5857): 1737-1742.
[2] Special report on the ocean and cryosphere in a changing climate [EB/OL]. [2025-05-23]. https: //www.ipcc.ch/srocc/.
[3] Rengasamy P. Soil processes affecting crop production in salt-affected soils [J]. Functional Plant Biology, 2010, 37(7): 613-620.

DOI: 10.54254/2753-8818/2026.HZ30831

[4] Shrivastava P, Kumar R. Soil salinity: A serious environmental issue and plant growth promoting bacteria as one of the tools for its alleviation [J]. Saudi journal of biological sciences, 2014, 22(2): 103.
[5] Vengosh A, Rosenthal E. Saline groundwater in Israel: its bearing on the water crisis in the country [J]. Journal of Hydrology, 1994, 156(1-4): 389-430.
[6] Boyd C E, Tucker C S. Pond aquaculture water quality management [M]. Springer Science & Business Media, 2010.
[7] Guidelines for drinking-water quality, 4th edition, incorporating the 1st addendum [EB/OL]. [2025-05-23]. https: //www.who.int/publications/i/item/9789241549950.
[8] Lagerloef G, Wentz F, Yueh S, et al.Aquarius satellite mission provides new, detailed view of sea surface salinity [J]. Bull. Am. Meteorol. Soc, 2010, 93(7): S70-S71.
[9] American Public Health Association. Standard methods for the examination of water and wastewater [M]. American public health association. 1926.
[10] Lumei Z, Zhong H, Huairen H, et al.Relationship Between the Refractive Index of Seawater and Salinity, Temperature [J].China Modern Educational Equipment, 2019.
[11] Koblinsky C J, Hildebrand P, LeVine D, et al. Sea surface salinity from space: Science goals and measurement approach [J]. Radio Science, 2003, 38(4): 29-1-29-2.
[12] Gabor D. A new microscopic principle [J]. 1948.
[13] Müller J, Kebbel V, Jüptner W. Digital holography as a tool for testing high-aperture micro-optics [J]. Optics and lasers in engineering, 2005, 43(7): 739-751.
[14] Coppola G, Ferraro P, Iodice M, et al.A digital holographic microscope for complete characterization of microelectromechanicalsystems [J]. Measurement Science and Technology, 2004, 15(3): 529.
[15] Mo X, Xie J, Zhang H, et al.Recoding and Dicoding Research of Digital Holographic Microscopy [J]. Transactions of Beijing institute of Technology, 2009 10: 902-905.
[16] Ma L, Wang H, Jin H, et al.Experimental study on quantitative phase imaging by digital holographic microscopy [J]. Zhongguo Jiguang(Chinese Journal of Lasers), 2010, 39(3): 0309002-7.
[17] Wang H, Liu F, Liao W, et al. Optimized digital micro-holographic imaging system [J]. Acta Physica Sinica, 2013, 62(5): 054208.
[18] Zuo C, Li J, Sun J, et al.Transport of intensity equation: a tutorial [J]. Optics and Lasers in Engineering, 2020, 135: 106187.